Nano Research
2019, 12(5): 1025–1031

ISSN 1998-0124 CN 11-5974/O4
https://doi.org/10.1007/s12274-019-2335-6

Research Article

Encapsulating segment-like antimony nanorod in hollow carbon tube as long-lifespan, high-rate anodes for rechargeable K-ion batteries

Wen Luo[1,§], Feng Li[2,§], Weiran Zhang[3], Kang Han[4], Jean-Jacques Gaumet[5], Hans-Eckhardt Schaefer[4,6], and Liqiang Mai[4] (✉)

[1] *Department of Physics, School of Science, Wuhan University of Technology, Wuhan 430070, China*
[2] *Hefei National Laboratory for Physical Sciences at the Microscale, University of Science and Technology of China, Hefei 230000, China*
[3] *Division of Materials Science and Engineering, Boston University, MA 02215, USA*
[4] *State Key Laboratory of Advanced Technology for Materials Synthesis and Processing, International School of Materials Science and Technology, Wuhan University of Technology, Wuhan 430070, China*
[5] *Laboratoire de Chimie et Physique: Approche Multi-échelles des Milieux Complexes, Institut Jean Barriol, Université de Lorraine, Metz 57070, France*
[6] *Institute for Functional Matter and Quantum Technologies, Stuttgart University, Pfaffenwaldring 57, Stuttgart 70569, Germany*
[§] *Wen Luo and Feng Li contributed equally to this work.*

Received: 12 December 2018 / **Revised:** 24 January 2019 / **Accepted:** 10 February 2019

ABSTRACT

K-ion battery (KIB) is a new-type energy storage device that possesses potential advantages of low-cost and abundant resource of potassium. To develop advanced electrode materials for accommodating the large size and high activity of potassium ion is of great interests. Herein, a segment-like antimony (Sb) nanorod encapsulated in hollow carbon tube electrode material (Sb@HCT) was prepared. Beneficial from the virtue of abundant nitrogen doping in carbon tube, one-dimensional and hollow structure advantages, Sb@HCT exhibits excellent potassium storage properties: in the case of potassium bis(fluorosulfonyl)imide (KFSI) electrolyte, Sb@HCT displays a reversible capacity of up to 453.4 mAh·g^{-1} at a current density of 0.5 A·g^{-1} and good rate performance (a capacity of 211.5 mAh·g^{-1} could be achieved at an ultrahigh rate of 5 A·g^{-1}). Additionally, Sb@HCT demonstrates excellent long-cycle stability at a current density of 2 A·g^{-1} over 120 cycles. Meanwhile, electrolyte optimization is an effective strategy for greatly improving electrochemical performance. Through *ex-situ* characterizations, we disclosed the potassiation of Sb anode is quite reversible and undergoes multistep processes, combining solid solution reaction and two-phase reaction.

KEYWORDS

K-ion battery, antimony anode, hollow carbon tube encapsulation, electrolyte optimization, potassium storage mechanism

1 Introduction

The fast growth in demand of clean and renewable energy resources, such as wind and solar energy requires the development of reliable energy storage devices with low cost, high safety, efficiency and exceptional performance. The lithium-ion battery (LIB) which has been predominantly used in electronic devices and electric vehicles and even in grid level storage, is regarded as one of most successful energy storage devices [1–6]. Nonetheless, the uneven global distribution and the limitation of lithium resources may significantly confine the sustainable application of LIB in the long term. In this view, rechargeable batteries employing sodium (Na) or potassium (K) instead of Li ions have gained increasing research interests because Na or K elements are geologically more abundant and cheaper than Li [7–9]. The high content of Na (23,000 ppm) and K (17,000 ppm) in the Earth's crust compared to the limited Li (20 ppm) makes it attractive to develop Na-ion battery (NIB) and K-ion battery (KIB) technologies [7, 8].

Recent studies [10–16] have demonstrated some attractive features of the KIB technology: the higher electrochemical potential of K/K$^+$ (–2.93 V vs. standard hydrogen electrode, SHE) or of Na/Na$^+$ (–2.71 V vs. SHE) compared to Li/Li$^+$ (–3.04 V vs. SHE) offers KIB a higher voltage plateau giving rise to an enhanced specific energy storage capability [17–19]. Additionally, electrolyte salt chemistry has shown that the nature of weak Lewis acids of K$^+$ ions in organic solvents can accelerate the kinetics and enhance the diffusion rate of K$^+$ ions [20–22].

Notably to date, recent efforts have been devoted to the success of high-performance KIB. The larger radius of K$^+$ ion (1.38 Å) relative to that of Li$^+$ ion (0.76 Å) or Na$^+$ ion (1.02 Å) motivated the exploration and design of suitable electrode materials to accommodate the huge volume variation during repeated K$^+$ ions uptake and release [13]. For the study of KIB electrode, alloying-type anodes, based on antimony [15], tin [23] or bismuth [21, 24], have captured substantial interests due to their suitable K$^+$ ion loading and unloading kinetics as well as their theoretical capacity higher than those of carbonaceous anodes with a theoretical capacity lower than 300 mAh·g^{-1} [25–27]. Thus, an anode material with a high K$^+$ ion storage capacity of 461 mAh·g^{-1} after 15 cycles at 200 mA·g^{-1} has been developed by using a composite of Sb nanoparticles in a carbon network [15]. A recent paper of employing Bi/rGO anode for KIB demonstrated graphene sheets worked as an excellent substrate to buffer volume changes of Bi nanoparticles during electrochemical cycles, thus this alloying-based Bi anode delivered a high

Address correspondence to mlq518@whut.edu.cn

reversible capacity of 290 mAh·g^{-1} after 50 cycles at 50 mA·g^{-1} [21].

Moreover, the overall electrochemical performance of rechargeable batteries can be improved by tuning the electrolyte [28–30]. For example, Wang et al. recently demonstrated that a high concentration of bis(fluorosulfonyl)imide anion (FSI^-) contributed interphases of high F content on both Li-metal anode and Ni-rich nickel-manganese-cobalt cathode surfaces, thus enabling high-voltage Li-metal batteries [31]. In the case of KIB, the introduction of potassium bis(fluorosulfonyl)imide (KFSI) favors the generation of more robust solid electrolyte interphase (SEI) layer and thus contributes to greatly enhanced potassium storage performance [21]. Meanwhile, SEI in the anode for KIBs with traditional electrolytes is mainly composed of organic compositions, which are highly reactive with air and water, resulting in inferior cycle performance. The electrolyte decomposition is likely resulted from KFSI due to the more reactive feature of KFSI salt confirmed by its calculated LUMO (lowest unoccupied molecular orbital) energy [32]. In this spirit, we report a novel high-performance anode for KIB consisting of segment-like antimony nanorods encapsulated in hollow carbon tubes (Sb@HCT). The combination of Sb nanorods, robust carbon coating layer and sufficient inner void architecture impacts to the Sb@HCT hybrid an excellent electrochemical reversibility and high charge/discharge rate capabilities. The use of KFSI salt as electrolyte further improves the overall electrochemical performance, especially the Coulombic efficiency and high-rate stability. The characterization of the anode material by *ex-situ* X-ray diffraction (XRD), Raman scattering and transmission electron microscopy (TEM) demonstrates a highly reversible potassium exchange in the Sb anode material via multistep processes combining solid solution reactions and two-phase reactions.

2 Results and discussions

The Sb@HCT anode was prepared according to our previous work [33]. Firstly, highly crystalline one-dimensional Sb_2S_3 nanorods (Fig. S1 in the Electronic Supplementary Material (ESM)) synthesized by a hydrothermal method possess uniform morphology with a diameter of about 90 nm and a length of hundreds of micrometers. Polypyrrole (PPy) was introduced to encapsulate Sb_2S_3 nanorods, in order to form the core-shell composite material Sb_2S_3@PPy. The XRD diffraction peaks of Sb_2S_3@PPy can be still indexed to the patterns of Sb_2S_3, which demonstrates that the polymer coating has no effect on the crystalline phase of Sb_2S_3 (Fig. S2(a) in the ESM). Sb_2S_3@PPy maintains 1D nanorods structure after the polymerization of pyrrole with a thickness of 15 nm (Figs. S2(b) and S2(c) in the ESM).The results of elemental mapping images reveal a uniform distribution of C, N, Sb, S elements (Figs. S2(d) and S2(e) in the ESM), implying the existence of PPy. By calcination the materials is transformed into Sb nanorods enclosed in carbon tubes. During the calcination-induced structural changes studied by XRD (Fig. S3(a) in the ESM), the characterisitic Sb_2S_3 signals diminish with calcination time increasing from 5 to 30 min, while the intensity of peaks ascribed to Sb gradually increase. After treatment of 45 min, only the diffraction peaks of Sb can be observed which fully correspond to standard pattern, suggesting the reaction of phase transformation fully occur. Even when the calcination time was extended to 60 min, pure, high-crystalline Sb maintained well. Meanwhile the morphology of samples after calcination treatment still retain 1D nanorods (Figs. S3(b)–S3(f) in the ESM). To retain relative high content of Sb in composite material, the materials after 45 min calcination was used for the subsequent studies.

The morphology of 1D Sb@HCT nanorods with a length of several micrometers, a diameter of around 100 nm can be characterized by SEM (Fig. 1(a)). As seen in Fig. 1(b), a structure of nanorod-in-nanotube with void space and a carbon layer of about 11 nm were obtained after annealing due to the volatilization, flow of Sb and

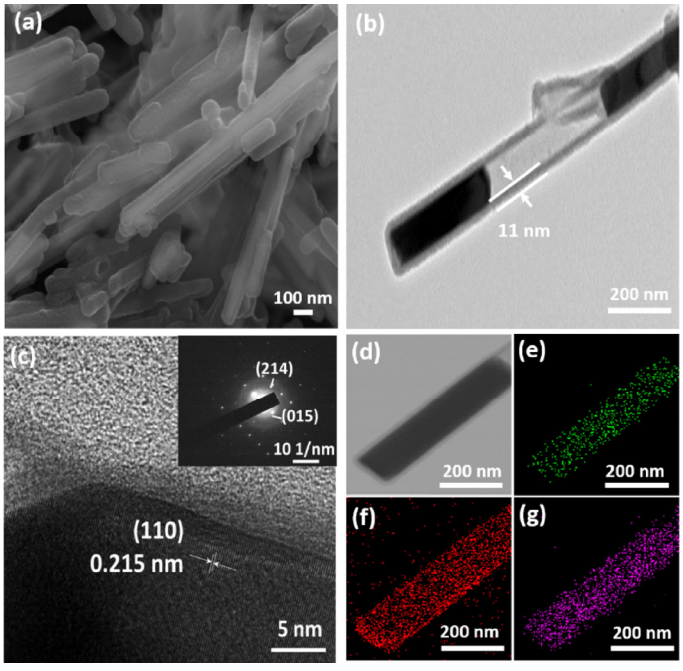

Figure 1 SEM image (a), TEM image (b), HRTEM image (c), SAED pattern (inset of (c)), TEM image (d) and corresponding element mapping image of Sb (e), C (f), N (g) of Sb@HCT.

the shrinkage of polymer. The high specific surface area of this morphology is confirmed by a Brunauer-Emmett-Teller (BET) analysis yielding a value of 14.8 m^2·g^{-1} (Fig. S4 in the ESM). It would facilitate an excellent contact of electrolyte with the electrode material. The lattice fringes observed by HRTEM with spacing of about 0.215 nm (Fig. 1(c)) correspond to the (110) planes of rhombohedral Sb as concluded from the selected area electron diffraction (SAED) pattern (inset of Fig. 1(c)). The element distribution of Sb, C, N from Fig. 1(d) shows that Sb is refined within tube, on the contrary, C and N are evenly distributed all through the entire carbon tube, indicating the peapod-like structure of Sb@HCT. Thermogravimetric analysis (TGA) demonstrates the content of Sb in the composite material can be calculated to be 60.8 wt.% (Fig. S5 in the ESM).

The local structure and carbon state information of Sb@HCT were studied by Raman measurement. The Raman data collected at a wavelength of 532 nm (Fig. 2(a)) distinctly disclosed the difference among pristine Sb_2S_3, Sb_2S_3@PPy and Sb@HCT. Three Raman peaks located at about 118, 190 and 255 cm^{-1} can be indexed with the typical characteristic vibration of Sb_2S_3 [34]. The intensity ratio of I_D to I_G of the D- and G-Raman bands of carbon at 1,365 and 1,580 cm^{-1} which represent the disordered and graphitized carbon, respectively [35], decreases upon calcination indicating the formation of graphitic carbon. Simultaneously, a Raman peak characteristic for elemental Sb appears at 150 cm^{-1} (Fig. 2(b)), signifying the formation of Sb nanorods [36]. The introduction of PPy into composite material is shown by the appearance of peaks in Fourier transform infrared spectroscopy (FTIR) located at 1,695, 1,550, 1,045 and 915 cm^{-1} which is correspond to C–N bond, C–C stretching, and the in-plane and out-plane deformation vibrations of C–H bond on the pyrrole ring, respectively (Fig. 2(c)) [37]. The disappearance of FTIR peaks of PPy indicates the disappearance of pyrrole ring structure due to carbon segregation by calcination.

By X-ray photoelectron spectroscopy (XPS) the electronic configurations of C and N atoms of Sb@HCT can be identified which may be of relevance for the electrical conductivity and the battery performance (Fig. 2(d)). It should be noted that the prominent oxygen feature signals come from the functional groups and water species on the sample surface. As shown in Fig. 2(e), two characteristic bands of the graphitic carbon (C=C) and C–C at 284.6 and 285.5 eV,

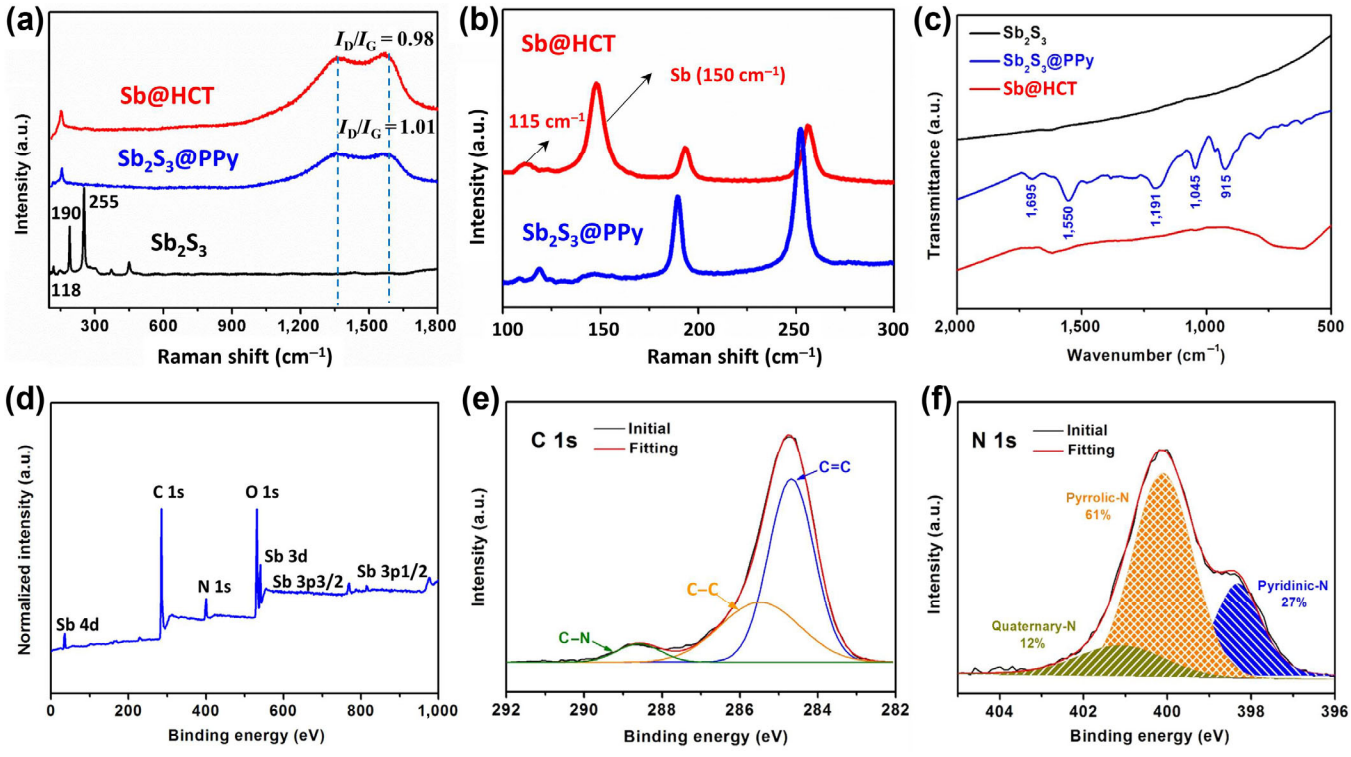

Figure 2 Raman spectra of Sb_2S_3, Sb_2S_3@PPy, Sb@HCT at an excitation wavelength of 532 nm (a), zoom-in Raman spectra of Sb_2S_3@PPy, Sb@HCT at an excitation wavelength of 633 nm (b), FTIR of Sb_2S_3, Sb_2S_3@PPy, Sb@HCT (c), XPS spectrum (d), high-resolution C 1s (e) and N 1s (f) of Sb@HCT.

respectively can be recognized from the high-resolution C 1s peaks [38]. The existence of C=C band indicates the graphitic structure of Sb@HCT, which significantly improved the electronic conductivity and electrochemical kinetics as reported in previous works [38, 39]. Moreover, the doping of N into carbon layer can be further proved by the observed bands of C–N at 288.6 eV. To clarify the kinds of N-doping, high-resolution N 1s spectrum was collected (Fig. 2(f)). There are three kinds of nitrogen namely pyridinic-N, pyrrolic-N and quaternary-N at 398.5, 400.1 and 401.1 eV, respectively doping into the carbon layer [39] with atomic ratios of 61:27:12. The abundant pyridinic-N, pyrrolic-N states as defects with free electron can accelerate ion diffusion so as to enhance electrochemical properties.

Sb@HCT was evaluated as an anode materials in a half-cell of KIB. Electrolyte adaption is pivotal for optimizing the electrochemical performance of alloying-based electrode materials. Recently, Guo et al. studied that FSI^- anion provided by KFSI salt can hamper the electrolyte decomposition and alter the surface passivation through the generation of a more durable SEI film, contributing to enhanced cycling performance [21]. Hereby, potassium hexafluorophosphate (KPF_6) or KFSI salt in ethylene carbon (EC)/dimethyl carbonate (DMC) (1:1 vol/vol) were studied to explore potassium storage performance. Figure 3(a) displays the cycling performance of Sb@HCT in KPF_6 and KFSI, respectively at a current density of 500 mA·g^{-1}. In the KPF_6 electrolyte, severe capacity decay occurs when the battery merely operates for a limited life of 30 cycles, and a low specific capacity of 73.5 mAh·g^{-1} can be delivered by Sb@HCT after 80 cycles. In contrast, Sb@HCT electrode in KFSI exhibits excellent cycling stability, retaining a reversible capacity up to 453.4 mAh·g^{-1} after 80 cycles with a high capacity retention of 84.0% (against 2nd discharge capacity). Besides, the Coulombic efficiency (CE) rapidly increases from about 70% to 99% after second cycle in KFSI electrolyte (Fig. 3(b)), whereas the CE fails to increase to 99% even after 5 cycles and cannot stabilize at about 99% during 80 cycles in KPF_6 electrolyte. These results illustrate the excellent cycling stability of Sb@HCT anode resulted from the synergistic effect of its structural design and the use of KFSI as an appropriate electrolyte salt.

In order to evaluate the cycling and rate behavior of Sb@HCT anode in the KIB, the discharge and charge capacities were measured in dependence of the current density (Fig. 3(c)). In KFSI, the average reversible capacity of Sb@HCT is 594.5, 526.5, 459.6, 386.3 and 316.9 mAh·g^{-1} with a stable CE of 99% during electrochemical reaction at a current density of 0.1, 0.2, 0.5, 1.0 and 2.0 A·g^{-1}, respectively. It is noteworthy that a capacity of 211.5 mAh·g^{-1} can be still retained at an ultrahigh current density of 5 A·g^{-1}. Moreover a discharge capacity of 400.5 mAh·g^{-1} is regained and retains stably in the follow cycles when the current density recovers to a lower current density of 0.1 A·g^{-1}. On the contrast in KPF_6, the overall output capacities are much lower than in the KFSI case: only a minor capacity of 94.0 mAh·g^{-1} can be reached at by applying a 5 A·g^{-1} current density, which is far below than the capacity (211.5 mAh·g^{-1}) attained in KFSI, demonstrating the superior rate capability of the robust Sb@HCT anode in the optimized KFSI electrolyte.

The cyclic voltammogram (CV) test was applied to analyze the potential of redox reaction during charging/discharging. Figure 3(d) shows the typical CV profiles of Sb@HCT anode during the first three cycles for KIB at a sweep rate of 0.2 mV·s^{-1}. A sharp peak centered at 0.55 V is ascribed to the alloying reaction between Sb and K forming K_3Sb species [15]. The two oxidation peaks at 0.66 and 1.20 V indicate the dealloying reaction is two-step process and an intermediate K_xSb phase may be generated, very similar to the reported Sb anode in NIB during the desodiation process [40, 41]. Specifically, the observed peaks can be assigned to the electrochemical oxidation of K_3Sb to form amorphous K_xSb and then Sb, respectively. With regards to CV curves collected from the KPF_6-based electrolyte, a broad peak at 0.42 V in the first cathodic scan is attributed to formation of the SEI film (Fig. S6 in the ESM). Different from the cases of those in KFSI, a noticeable tail peak at the first anodic scan, which disappeared in the subsequent scans, is ascribed to unstable nature of KPF_6 at higher voltage. The curves of the following tests match with the first cycle, demonstrating the reversibility and stability of Sb@HCT anode. Furthermore, the discharge profiles of Sb@HCT display the obvious plateau around 0.60 V which is in

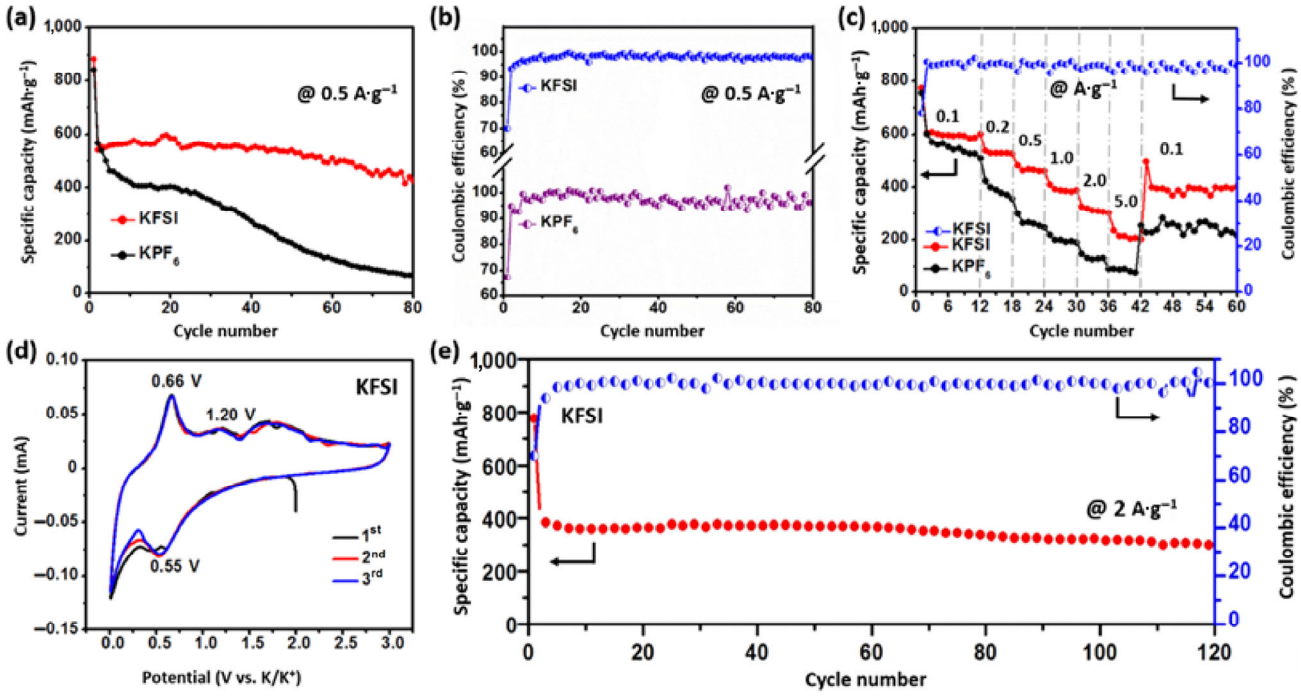

Figure 3 Electrochemical performances of Sb@HCT as an anode in KIB. Cycling performance of Sb@HCT in KFSI and KPF_6 electrolyte at 0.5 $A·g^{-1}$ (a) and corresponding Coulombic efficiency (b), rate performance of Sb@HCT in KFSI and KPF_6 electrolyte (c), CV curves (d) and long-term cycling performance of Sb@HCT in KFSI electrolyte at 2 $A·g^{-1}$ (e).

accordance with afore-discussed CV results (Fig. S7 in the ESM). Besides, electrochemical impedance spectroscopy (EIS) measurement of Sb@HCT was employed before cycling (Fig. S8 in the ESM). The EIS plots of Sb@HCT anode in two different electrolyte systems possess similar profiles in both low and high frequency regions, which implies the electrolyte salt has little effects on the charge transfer and conductivity of electrode at the initial state.

Figure 3(e) further evaluates the long-term cycling performance of Sb@HCT. At a high current density of 2 $A·g^{-1}$, after 120 cycles, Sb@HCT anode can still deliver a high capacity of 300.1 $mAh·g^{-1}$ with the capacity retention of 73.5% (against the reversible capacity of second cycle). Considering high reversible capacity, high-rate performance and long-term stability, the Sb@HCT anode exhibits an impressive electrochemical performance exceeding those of other alloy-based anodes (Table S1 in the ESM), suggesting its promising potential in the application for high-performance KIB.

The potassiation/depotassiation mechanism of Sb@HCT anode can be further elucidated by *ex-situ* XRD, Raman and TEM studies in various states in the first cycle after disassembling the cell. When discharging to 0.4 V (Fig. 4, state II), the initial Raman modes of Sb partially disappear and the Raman signature observed in the discharged state II is assigned to K_xSb [36] which appears to be amorphous since no diffraction signal is found in XRD. However, the diffraction peaks of Sb remain and shift to higher 2θ degree with a narrower full-width half-maximum (FWHM) characteristic, implying that Sb undergoes a solid-solution reaction whereby Sb(K) phase with smaller size might be formed. Similar observation on the lattice shrinkage as a result of potassium intercalation were also reported in the case of Bi anode for NIB [42] and KIB [21], respectively. Upon further discharging to 0.01 V, a broad Raman peak located at 164 cm^{-1} which is assigned to K_3Sb could be observed [43, 44]. Notably, no XRD signals from K_3Sb are detected

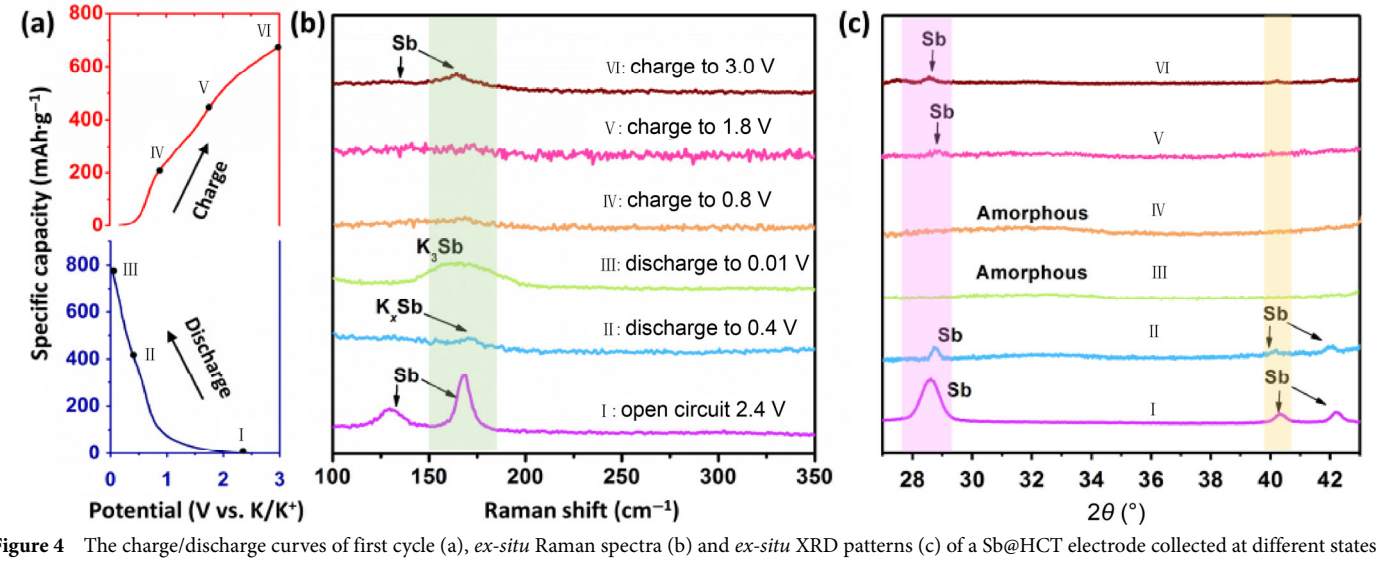

Figure 4 The charge/discharge curves of first cycle (a), *ex-situ* Raman spectra (b) and *ex-situ* XRD patterns (c) of a Sb@HCT electrode collected at different states at a current density of 0.5 $A·g^{-1}$.

due to its possible low-crystalline or amorphous feature of the final discharging product. When recharging to 0.8 V, almost no signal is collected in both Raman spectrum and XRD pattern. Still charging to 1.8 V, Sb phase would be possibly formed by the evidence of a very weak XRD peak located around 28.7°, which nevertheless is not detected in Raman spectrum probably owing to its low amount and nanocrystalline nature. At the end of charge, it is obviously clear to see the emergence of Raman modes and XRD peaks ascribed to metallic Sb are captured.

TEM and SAED analyses of the Sb@HCT anode material after disassembling the cell at different charge/discharge states show that when discharging to 0.4 V, Sb materials disintegrated to Sb nanocrystals (Figs. 5(b) and 5(c)) within intact carbon tubes (Fig. 5(a)). The HRTEM image verifies the formation of Sb nanograins with average size of ~ 5 nm (Fig. 5(c)). The lattice fringes with spacing of 0.21 and 0.31 nm which respectively correspond to the (110) and (012) planes of rhombohedral Sb can be clearly observed (Fig. 5(c)). The above TEM results confirm that Sb experiences a solid-solution reaction and forms Sb(K) phase (while remains the same asymmetry) would result in moderate lattice shrinkage, in accordance with above *ex-situ* XRD results. At fully discharging state, although slight expansion of carbon tube and localized separation of Sb are observed (Fig. 5(d)), the carbon layer can well accommodate the large volume expansion and thus maintain its 1D structure. The typical diffraction rings correspond to plane spacing of 0.211 and 0.124 nm, respectively, which is consistent with the (203) and (306) planes of hexagonal K_3Sb. Moreover, a weak diffraction ring with a spacing of 0.332 nm corresponds to (112) plane of monoclilic K_5Sb_4 is also detected, suggesting the high concentration uptake of potassium in the anode. Upon recharging to 0.8 V, amorphous ring halos in SAED pattern (inset of Fig. 5(f)) taken from the charged Sb@HCT region with characteristics of K_xSb. After charging to 1.8 V, Sb nanocrystallites are formed inside intact carbon tubes within localized area as identified by SAED (Fig. 5(g) and inset) and earlier observed by XRD (see above). Moreover, the measured lattice spacing is smaller relative to that of pristine Sb, suggesting a reversible lattice shrinkage also happens during the extraction of potassium ion. Proceeding to a fully depotassiation state of 3.0 V, the encapsulation structure maintain intact well (Fig. 5(h)) and the diffraction rings of metallic Sb clearly emerge (Fig. 5(i)).

To recap, the reaction mechanism of Sb@HCT anode is schematically illustrated in Fig. 6. During alloying reaction, Sb@HCT first experiences a solid-solution reaction and forms Sb(K) associated with the structural evolution from segment-like Sb nanorod into localized Sb nanograins; then through a two-phase reaction, hexagonal K_3Sb and probably a trace amount of low-crystalline K_5Sb_4, at least in our case, are generated in the finally discharge product. Upon dealloying, highly reversible two-phase reaction and

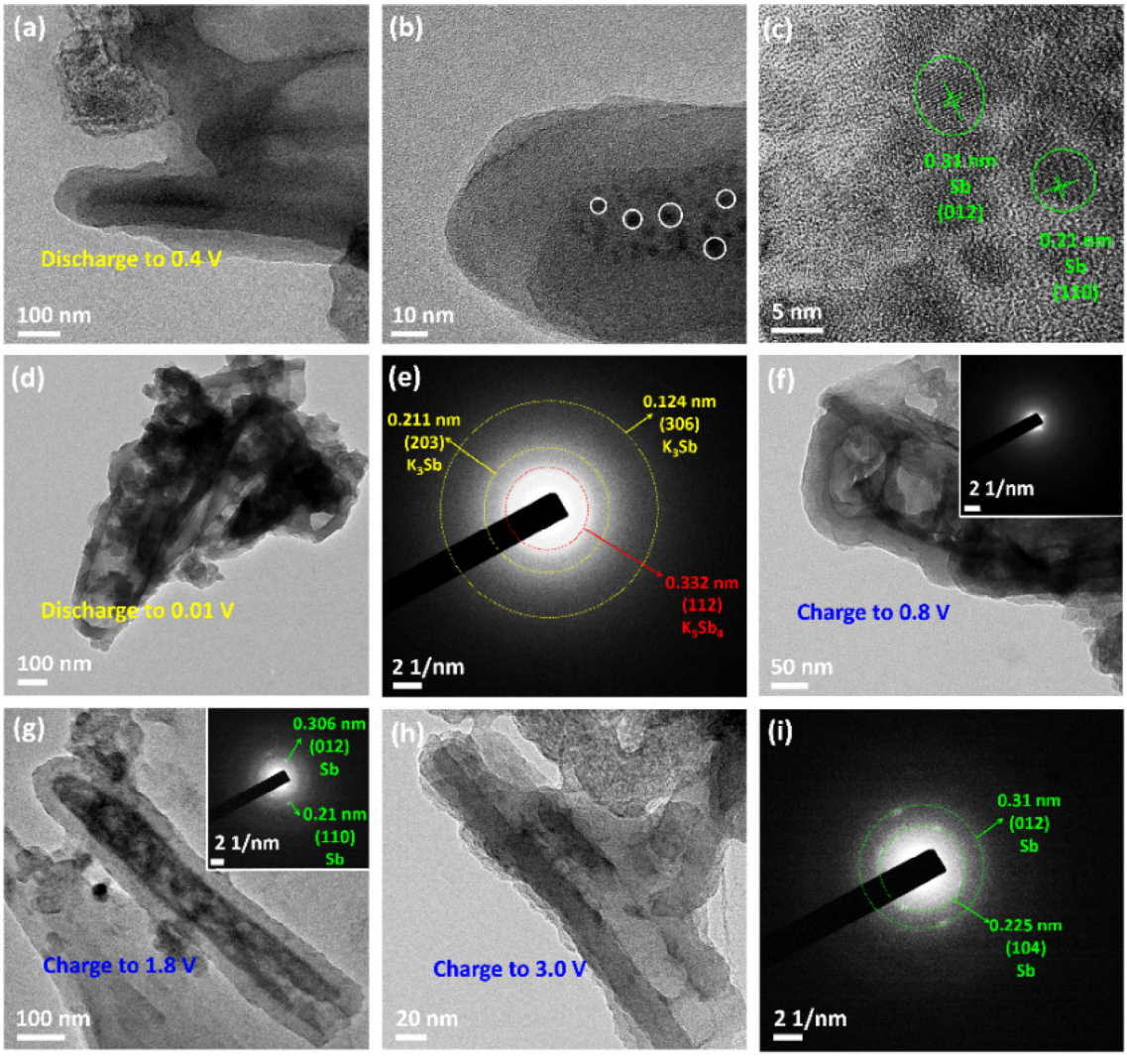

Figure 5 *Ex-situ* TEM characterization of Sb@HCT collected at different states during the first discharge/charge cycle at a current density of 0.5 $A \cdot g^{-1}$: TEM images ((a) and (b)) and HRTEM image (c) when discharging to 0.4 V. TEM image (d) and SAED patterns (e) when discharging to 0.01 V. TEM image (f) and SAED patterns (inset of (f)) when charging to 0.8 V. TEM image (g) and SAED patterns (inset of (g)) when charging to 1.8 V. TEM image (h) and SAED patterns (i) when charging to 3.0 V.

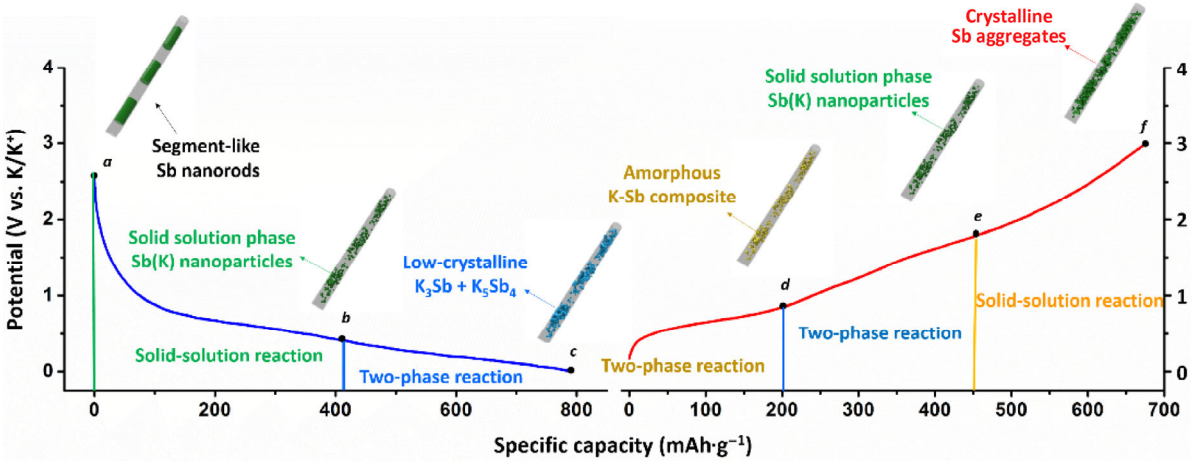

Figure 6 Schematic illustration of the reaction mechanism of Sb@HCT as an anode in KIB.

solid solution reaction take place in sequence, whereby amorphous intermediate products and finally crystalline, localized Sb aggregates are evidenced. Overall, owing to the unique, robust hollow carbon tube encapsulation structure and electrolyte salts chemistry, Sb@HCT demonstrates a highly reversible potassiation/depotassiation process.

3 Conclusions

In conclusion a novel structure of Sb nanorod encapsulated in nanotube (Sb@HCT) was fabricated as a KIB anode. The introduction of KFSI as an electrolyte salt functions as an effective strategy for greatly boosting electrochemical performance. In virtue of hollow structure (to accommodate volume expansion), N-doping carbon coating layer (to promote conductivity) and the effect of KFSI (to favor the generation of robust SEI), Sb@HCT anode displays a high-rate capacity of 211.5 mAh·g^{-1} at an ultrahigh current density of 5 A·g^{-1} and a long lifespan with a capacity of 300.1 mAh·g^{-1} even after 120 cycles at 2 A·g^{-1}. *Ex-situ* XRD, Raman and TEM characterizations indicate that Sb@HCT undergoes a reversible alloying/ dealloying process whereby solid-solution reaction and two-phase reaction take place in sequence. The tube-like nanostructure and the adaption of the electrolyte salt efficiently can be extended to enhance the electrochemical performance of alloying-based electrode materials for energy storage.

Acknowledgements

We thank Prof. Hans-Eckhardt Schaefer (Stuttgart University) for stimulating discussions and English editing of the manuscript. This work was supported by the National Natural Science Foundation of China (No. 51832004), the National Natural Science Fund for Distinguished Young Scholars (No. 51425204), the National Key R&D Program of China (No. 2016YFA0202603), the Programme of Introducing Talents of Discipline to Universities (No. B17034), and the Yellow Crane Talent (Science & Technology) Program of Wuhan City.

Electronic Supplementary Material: Supplementary material (experimental, TGA, SEM, XRD and performance comparison) is available in the online version of this article at https://doi.org/10.1007/s12274-019-2335-6.

References

[1] Tarascon, J. M.; Armand, M. Issues and challenges facing rechargeable lithium batteries. *Nature* **2001**, *414*, 359–367.
[2] Mai, L. Q.; Yan, M. Y.; Zhao, Y. L. Track batteries degrading in real time. *Nature* **2017**, *546*, 469–470.
[3] Goodenough, J. B.; Kim, Y. Challenges for rechargeable Li batteries. *Chem. Mater.* **2010**, *22*, 587–603.
[4] Zhou, H. J.; Zhao, H. B.; Zhang, X.; Cheng, H. W.; Lu, X. G.; Xu, Q. Facile one-step synthesis of Cu_2O@Cu sub-microspheres composites as anode materials for lithium ion batteries. *J. Mater. Sci. Technol.* **2018**, *34*, 1085–1090.
[5] Wu, G.; More, K. L.; Xu, P.; Wang, H. L.; Ferrandon, M.; Kropf, A. J.; Myers, D. J.; Ma, S. G.; Johnston, C. M.; Zelenay, P. A carbon-nanotube-supported graphene-rich non-precious metal oxygen reduction catalyst with enhanced performance durability. *Chem. Commun.* **2013**, *49*, 3291–3293.
[6] Jiao, Y. C.; Han, D. D.; Ding, Y.; Zhang, X. F.; Guo, G. N.; Hu, J. H.; Yang, D.; Dong, A. G. Fabrication of three-dimensionally interconnected nanoparticle superlattices and their lithium-ion storage properties. *Nature Commun.* **2015**, *6*, 6420.
[7] Gao, H.; Zhou, T. F.; Zheng, Y.; Zhang, Q.; Liu, Y. Q.; Chen, J.; Liu, H. K.; Guo, Z. P. CoS quantum dot nanoclusters for high-energy potassium-ion batteries. *Adv. Funct. Mater.* **2017**, *27*, 1702634.
[8] Luo, W.; Calas, A.; Tang, C. J.; Li, F.; Zhou, L.; Mai, L. Q. Ultralong Sb_2Se_3 nanowire-based free-standing membrane anode for lithium/sodium ion batteries. *ACS Appl. Mater. Interfaces* **2016**, *8*, 35219–35226.
[9] He, Y. Z.; Han, X. J.; Du, Y. C.; Song, B.; Zhang, B.; Zhang, W.; Xu, P. Conjugated polymer-mediated synthesis of sulfur- and nitrogen-doped carbon nanotubes as efficient anode materials for sodium ion batteries. *Nano Res.* **2018**, *11*, 2573–2585.
[10] Lakshmi, V.; Chen, Y.; Mikhaylov, A. A.; Medvedev, A. G.; Sultana, I.; Rahman, M. M.; Lev, O.; Prikhodchenko, P. V.; Glushenkov, A. M. Nano-crystalline SnS_2 coated onto reduced graphene oxide: Demonstrating the feasibility of a non-graphitic anode with sulfide chemistry for potassium-ion batteries. *Chem. Commun.* **2017**, *53*, 8272–8275.
[11] Slater, M. D.; Kim, D.; Lee, E.; Johnson, C. S. Sodium-ion batteries. *Adv. Funct. Mater.* **2013**, *23*, 947–958.
[12] Wang, X. P.; Xu, X. M.; Niu, C. J.; Meng, J. S.; Huang, M.; Liu, X.; Liu, Z.; Mai, L. Q. Earth abundant Fe/Mn-based layered oxide interconnected nanowires for advanced K-ion full batteries. *Nano Lett.* **2017**, *17*, 544–550.
[13] Zhang, W. C.; Mao, J. F.; Li, S. A.; Chen, Z. X.; Guo, Z. P. Phosphorus-based alloy materials for advanced potassium-ion battery anode. *J. Am. Chem. Soc.* **2017**, *139*, 3316–3319.
[14] McCulloch, W. D.; Ren, X. D.; Yu, M. Z.; Huang, Z. J.; Wu, Y. Y. Potassium-ion oxygen battery based on a high capacity antimony anode. *ACS Appl. Mater. Interfaces* **2015**, *7*, 26158–26166.
[15] Han, C. H.; Han, K.; Wang, X. P.; Wang, C. Y.; Li, Q.; Meng, J. S.; Xu, X. M.; He, Q.; Luo, W.; Wu, L. M. et al. Three-dimensional carbon network confined antimony nanoparticle anodes for high-capacity K-ion batteries. *Nanoscale* **2018**, *10*, 6820–6826.
[16] Xie, Y. H.; Chen, Y.; Liu, L.; Tao, P.; Fan, M. P.; Xu, N.; Shen, X. W.; Yan, C. L. Ultra-high pyridinic N-doped porous carbon monolith enabling high-capacity K-ion battery anodes for both half-cell and full-cell applications. *Adv. Mater.* **2017**, *29*, 1702268.
[17] Naguib, M.; Adams, R. A.; Zhao, Y. P.; Zemlyanov, D.; Varma, A.; Nanda, J.; Pol, V. G. Electrochemical performance of MXenes as K-ion battery anodes. *Chem. Commun.* **2017**, *53*, 6883–6886.

[18] Wang, X. P.; Han, K.; Wang, C. Y.; Liu, Z. A; Xu, X. M.; Huang, M.; Hu, P.; Meng, J. S.; Li, Q.; Mai, L. Q. Graphene oxide-wrapped dipotassium terephthalate hollow microrods for enhanced potassium storage. *Chem. Commun*. **2018**, *54*, 11029–11032.
[19] Jian, Z. L.; Luo, W.; Ji, X. L. Carbon electrodes for K-ion batteries. *J. Am. Chem. Soc*. **2015**, *137*, 11566–11569.
[20] Xue, L. G.; Li, Y. T.; Gao, H. C.; Zhou, W. D.; Lü, X. J.; Kaveevivitchai, W.; Manthiram, A.; Goodenough, J. B. Low-cost high-energy potassium cathode. *J. Am. Chem. Soc*. **2017**, *139*, 2164–2167.
[21] Zhang, Q.; Mao, J. F.; Pang, W. K.; Zheng, T.; Sencadas, V.; Chen, Y. Z.; Liu, Y. J.; Guo, Z. P. Boosting the potassium storage performance of alloy-based anode materials via electrolyte salt chemistry. *Adv. Energy Mater*. **2018**, *8*, 1703288.
[22] Okoshi, M.; Yamada, Y.; Komaba, S.; Yamada, A.; Nakai, H. Theoretical analysis of interactions between potassium ions and organic electrolyte solvents: A comparison with lithium, sodium, and magnesium ions. *J. Electrochem. Soc*. **2017**, *164*, A54–A60.
[23] Sultana, I.; Ramireddy, T.; Rahman, M. M.; Chen, Y.; Glushenkov, A. M. Tin-based composite anodes for potassium-ion batteries. *Chem. Commun*. **2016**, *52*, 9279–9282.
[24] Lei, K. X.; Wang, C. C.; Liu, L. J.; Luo, Y. W.; Mu, C. N.; Li, F. J.; Chen, J. A porous network of bismuth used as the anode material for high-energy-density potassium-ion batteries. *Angew. Chem., Int. Ed*. **2018**, *130*, 4777–4781.
[25] Wang, W.; Zhou, J. H.; Wang, Z. P.; Zhao, L. Y.; Li, P. H.; Yang, Y.; Yang, C.; Huang, H. X.; Guo, S. J. Short-range order in mesoporous carbon boosts potassium-ion battery performance. *Adv. Energy Mater*. **2018**, *8*, 1701648.
[26] Zhao, J.; Zou, X. X.; Zhu, Y. J.; Xu, Y. H.; Wang, C. S. Electrochemical intercalation of potassium into graphite. *Adv. Funct. Mater*. **2016**, *26*, 8103–8110.
[27] Luo, W.; Wan, J. Y.; Ozdemir, B.; Bao, W. Z.; Chen, Y. N.; Dai, J. Q.; Lin, H.; Xu, Y.; Gu, F.; Barone, V. et al. Potassium ion batteries with graphitic materials. *Nano Lett*. **2015**, *15*, 7671–7677.
[28] Gao, Y.; Yi, R.; Li, Y. C.; Song, J. X.; Chen, S. R.; Huang, Q. Q.; Mallouk, T. E.; Wang, D. H. General method of manipulating formation, composition, and morphology of solid-electrolyte interphases for stable Li-alloy anodes. *J. Am. Chem. Soc*. **2017**, *139*, 17359–17367.
[29] Lei, K. X.; Li, F. J.; Mu, C. N.; Wang, J. B.; Zhao, Q.; Chen, C. C.; Chen, J. High K-storage performance based on the synergy of dipotassium terephthalate and ether-based electrolytes. *Energy Environ. Sci*. **2017**, *10*, 552–557.
[30] Madec, L.; Gabaudan, V.; Gachot, G.; Stievano, L.; Monconduit, L.; Martinez, H. Paving the way for K-ion batteries: Role of electrolyte reactivity through the example of Sb-based electrodes. *ACS Appl. Mater. Interfaces* **2018**, *10*, 34116–34122.
[31] Fan, X. L.; Chen, L.; Ji, X.; Deng, T.; Hou, S.; Chen, J.; Zheng, J.; Wang, F.; Jiang, J. J.; Xu, K. et al. Highly fluorinated interphases enable high-voltage Li-metal batteries. *Chem* **2018**, *4*, 174–185.
[32] Fan, L.; Chen, S. H.; Ma, R. F.; Wang, J.; Wang, L. L.; Zhang, Q. F.; Zhang, E. J.; Liu, Z. M.; Lu, B. G. Ultrastable potassium storage performance realized by highly effective solid electrolyte interphase layer. *Small* **2018**, *14*, 1801806.
[33] Luo, W.; Li, F.; Gaumet, J. J.; Magri, P.; Diliberto, S.; Zhou, L.; Mai, L. Q. Bottom-up confined synthesis of nanorod-in-nanotube structured Sb@N-C for durable lithium and sodium storage. *Adv. Energy Mater*. **2018**, *8*, 1703237.
[34] Xiong, X. H.; Wang, G. H.; Lin, Y. W.; Wang, Y.; Ou, X.; Zheng, F. H.; Yang, C. H.; Wang, J. H.; Liu, M. L. Enhancing sodium ion battery performance by strongly binding nanostructured Sb_2S_3 on sulfur-doped graphene sheets. *ACS Nano* **2016**, *10*, 10953–10959.
[35] Luo, W.; Zhang, P. F.; Wang, X. P.; Li, Q. D.; Dong, Y. F.; Hua, J. C.; Zhou, L.; Mai, L. Q. Antimony nanoparticles anchored in three-dimensional carbon network as promising sodium-ion battery anode. *J. Power Sources* **2016**, *304*, 340–345.
[36] McGuire, K.; Lowhorn, N. D.; Tritt, T. M.; Rao, A. M. Raman scattering in doped transition metal pentatellurides. *J. Appl. Phys*. **2002**, *92*, 2524–2527.
[37] Wang, S.; Yuan, S.; Yin, Y. B.; Zhu, Y. H.; Zhang, X. B.; Yan, J. M. Green and facile fabrication of MWNTs@Sb_2S_3@PPy coaxial nanocables for high-performance Na-ion batteries. *Part. Part. Syst. Char*. **2016**, *33*, 493–499.
[38] Fu, L. J.; Tang, K.; Song, K. P.; van Aken, P. A.; Yu, Y.; Maier, J. Nitrogen doped porous carbon fibres as anode materials for sodium ion batteries with excellent rate performance. *Nanoscale* **2014**, *6*, 1384–1389.
[39] Shen, W.; Wang, C.; Xu, Q. J.; Liu, H. M.; Wang, Y. G. Nitrogen-doping-induced defects of a carbon coating layer facilitate Na-storage in electrode materials. *Adv. Energy Mater*. **2015**, *5*, 1400982.
[40] Darwiche, A.; Marino, C.; Sougrati, M. T.; Fraisse, B.; Stievano, L.; Monconduit, L. Better cycling performances of bulk Sb in Na-ion batteries compared to Li-ion systems: An unexpected electrochemical mechanism. *J. Am. Chem. Soc*. **2012**, *134*, 20805–20811.
[41] He, M.; Kravchyk, K.; Walter, M.; Kovalenko, M. V. Monodisperse antimony nanocrystals for high-rate Li-ion and Na-ion battery anodes: Nano versus bulk. *Nano Lett*. **2014**, *14*, 1255–1262.
[42] Su, D. W.; Dou, S. X.; Wang, G. X. Bismuth: A new anode for the Na-ion battery. *Nano Energy* **2015**, *12*, 88–95.
[43] Yi, Z.; Lin, N.; Zhang, W. Q.; Wang, W. W.; Zhu, Y. C.; Qian, Y. T. Preparation of Sb nanoparticles in molten salt and their potassium storage performance and mechanism. *Nanoscale* **2018**, *10*, 13236–13241.
[44] Tzolov, M. B.; Iliev, M. N. Raman scattering from monoalkali (Na-Sb and K-Sb), bialkali (Na-K-Sb) and multialkali (Na-K-Sb-Cs) photocathodes. *Thin Solid Films* **1992**, *213*, 99–102.